LLNL-TR-735228

Theory, Solution Methods, and Implementation of the HERMES Model

J. E. Reaugh, B. W. White, J. P. Curtis, H. K. Springer

July 21, 2017

Disclaimer

This work performed under the auspices of the U.S. Department of Energy by Lawrence Livermore National Laboratory under Contract DE-AC52-07NA27344.

Theory, Solution Methods, and Implementation of the HERMES Model

John E. Reaugh,[1] Bradley W. White,[1] John P. Curtis, [2,3] and H. Keo Springer[1]

[1]*Lawrence Livermore National Laboratory, 7000 East Avenue, Livermore, CA 94550, USA*
[2]*Atomic Weapons Establishment Aldermaston, RG7 4PR, Reading, Berkshire, UK*
[3]*Department of Mathematics, University College London, Gower Street, London, WC1E 6BT, UK*

The HERMES (high explosive response to mechanical stimulus) model was developed over the past decade to enable computer simulation of the mechanical and subsequent energetic response of explosives and propellants to mechanical insults such as impacts, perforations, drops, and falls. The model is embedded in computer simulation programs that solve the non-linear, large deformation equations of compressible solid and fluid flow in space and time. It is implemented as a user-defined model, which returns the updated stress tensor and composition that result from the simulation supplied strain tensor change. Although it is multi-phase, in that gas and solid species are present, it is single-velocity, in that the gas does not flow through the porous solid. More than 70 time-dependent variables are made available for additional analyses and plotting. The model encompasses a broad range of possible responses: mechanical damage with no energetic response, and a continuous spectrum of degrees of violence including delayed and prompt detonation. This paper describes the basic workings of the model.

I. INTRODUCTION

The HERMES model was developed to describe the circumstances under which explosives or propellants undergo a rapid release of energy following a mechanical insult. The model has been applied to the analysis of accidents (Hazards assessment), to a suite of standardized tests used to assess whether a system can be designated an Insensitive Munition (IM assessment), and to laboratory-scale experimental test vehicles. At present, it is not a fully predictive model, whose results could be used in the absence of testing. Instead HERMES is best used as a guide for understanding the results of testing, as an aid for designing new tests, and for identifying key mechanisms that contribute most to the reaction violence in a specific scenario.

Fundamental to our model is the interplay between damage in the explosive and the violence of the energetic response. Mechanical insults produce damage, which is manifest as surface area by the creation of cracks and fragments, and as porosity by the separation of crack faces and isolation of the fragments. As the kinetic energy and power of the insult increases, the degree of damage and the volume of damage both increase. After a localized ignition (see Sec. IV.A), open porosity permits a flame to spread easily throughout the damaged volume and ignite the newly formed surface area. The additional surface area leads to a proportional increase in the mass-burning rate. The pressure increases at an accelerating rate, because the burn velocity is pressure dependent. If neither mechanical strength nor inertial confinement can successfully contain the pressure, the surrounding materials begin to expand. The expansion of a confining structure can produce a metal fragment field, and the expansion of gas products can produce air blast. Both of these consequences can be used as measures of violence for the event. At the same time, the expansion reduces the pressure, slows the further production of gas product, and may even extinguish the flame. Under circumstances of high confinement, whether from material strength or the inertia of a large mass, pressure may build up rapidly enough that a shock wave is propagated into the surrounding unburned explosive. In some cases, this may lead to the development of a delayed detonation, DDT (deflagration-to-detonation transition). If the confining structure is weaker, unburned but fragmented explosive may be ejected away from the burning material. If that cloud of unburned fragments hits a nearby solid, a stopping shock will develop in the cloud that may lead to a delayed detonation, XDT (x for unknown cause of detonation transition). XDT is now generally believed to be caused by the shock recompaction of damaged, porous material, leading to a detonation that may spread to the nearby, undamaged explosive or propellant. Our model is intended to be useful for performing computer simulations of the entire spectrum of energetic response.

There are three main components of the model: pressure equilibration between the reactant and gas products (Sec. II), mechanical strength and failure of the solid reactant (Sec. III), and rate laws that determine the composition (reactant and gas product) as it evolves in time and space (Sec. IV). We conclude by describing previous and potential future applications of HERMES, and assessing its capabilities and shortcomings. (Sec. V)

II. CALCULATION OF PRESSURE

In computational studies of DDT (Baer and Nunziato 1986, Lapela *et al.* 2001), and interior ballistics (Gough and Zwarts 1979), the stress tensor of the mixture has contribution from both the gas and the solid phases. At low porosity, there can be stress in the solid due to stress bridging in the skeleton/matrix that surrounds the gas-filled pores, even when the gas pressure is nil. Any gas pressure adds to the total stress tensor. In the rock and soil mechanics literature, the stress in the matrix that exceeds the pressure in the intervening fluid (water) is called the effective stress (Terzaghi *et al.* 1996, p83), and the strength of the matrix is assumed to depend on the effective stress. If the porosity is so high that the particles lose contact, there is no longer a contribution to the pressure from stress bridging in the matrix and the composite has no strength. Figure 1 illustrates the differences between low porosity (left) and high porosity (right). In our model, the gas and solid phases are present at the initial time. The initial porosity of the explosive is filled with product gas at the initial conditions, usually 1 bar and 298K.

A. Equation of state of the gas products

We use the thermodynamic chemical equilibrium solver Cheetah (Fried *et al.* 2002, Bastea *et al.* 2006) to develop an equation of state table for the equilibrium composition of the gas products. Once the constituents of the explosive are determined, our table is constructed by calculating the pressure and internal energy density for a set of isotherms over a range of densities. Typically, our density range is 10^{-6} to 3.5 g/cc, and our temperature range is 290 to 30,000K. Our interpolations in the table are logarithmic in density and pressure, and linear in internal energy density and temperature. We permit extrapolation in density, but force the temperature to be no lower than the lowest temperature entry and no higher than the highest entry.

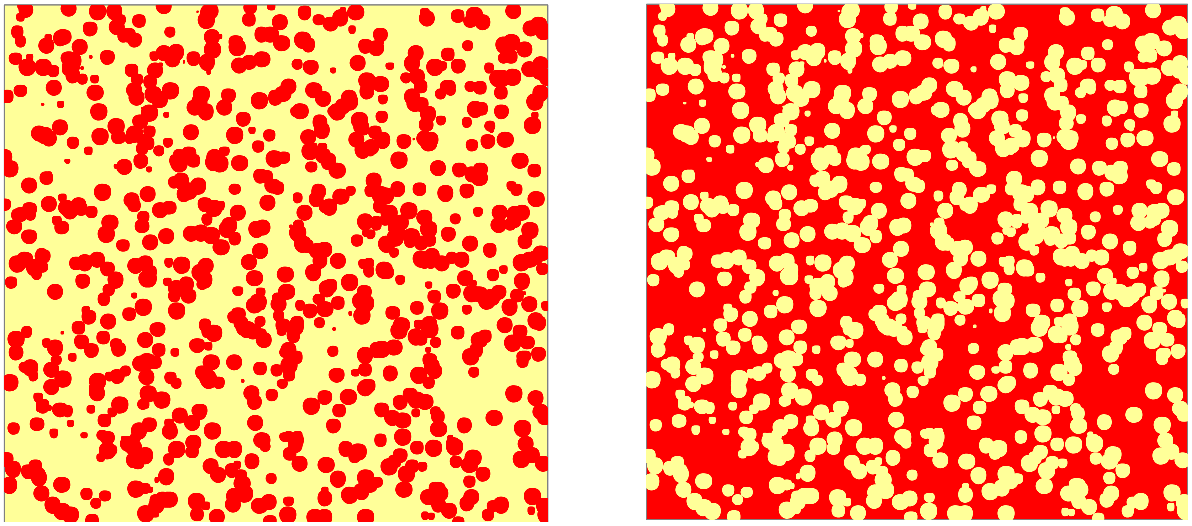

Figure 1. Illustration of low porosity (25% by volume, left), where stress-bridging can occur from one side of the cross section to the other in the connected matrix of solid (yellow or light) and high porosity (75% by volume, right), where the individual particles of solid (yellow or light) are in pressure equilibrium with the surrounding gas product (red or dark).

The critical point temperature of the gas product mixture is often below 500K. As a consequence, the gas-fluid coexistence region is then located within the boundaries of our table. The recent addition (Cheetah v.8) of liquid phase species of water, carbon dioxide and ammonia have dramatically improved the behavior in this region for CHNO explosives by reducing and/or eliminating Van der Waals loops. However, in some cases, changes in the condensed phase or gas composition on an isotherm can lead to non-monotonic behavior (kinks). If a kink is observed, we use a smooth approximation for the isotherms. We connect a pressure-density point on the high-density side of the kink and a point on the low-density side with a straight line in (log-density, log-pressure) space and (log-density, energy density) space. This fosters convergence of our iteration for pressure equilibrium.

To calculate the gas pressure for a density, specific internal energy pair, we interpolate the pressure and density logarithmically and the specific energy and temperature linearly. The gas energy density is tabulated as relative to the reactant at STP. As a result, transformation of reactant to product is not accompanied by any “energy of reaction”. Rather the energy density of the gas products at STP have a large negative value. As an example, the products of a TNT detonation expanded to STP have an energy density of -1000 cal/g in our table, which corresponds to the conventional explosive yield of TNT without afterburn, 1000 cal/g. With this convention, there is no change in the internal energy density for a conversion of reactant to product at constant volume.

B. Equation of state of the solid

We use a Mie-Grüneisen equation of state for the solid pressure, P_s.

$$P_s = P_{ad}\,(v_s) + \frac{\Gamma}{v_s}\,[e - e_{ad}(v_s)] \tag{1}$$

where P_{ad} is the pressure on the adiabat from room temperature and pressure, v_s is the specific volume of the solid, Γ is the Grüneisen coefficient and e_{ad} is the specific energy (energy per unit mass) on the adiabat, and where

$$P_{ad} = -\frac{\partial e_{ad}}{\partial v_s} \tag{2}$$

The pressure on the adiabat is given by a low-order polynomial in excess compression. It is convenient for us to use the adiabat as the reference curve for the solid (and also the skeleton/matrix in Section C below) because we are implementing a version of CREST (Handley, 2006) for the conversion rate of reactant to gas product in a detonation. (See Sec. IV.D) That model uses a measure of entropy as the dependent variable, for which the principal adiabat is the reference state.

$$P_{ad} = A_1\mu + A_2\mu^2 + A_3\mu^3 \tag{3}$$

where

$$\mu = \frac{1}{v_s\rho_0} - 1 \tag{4}$$

The parameter ρ_0 is the reference state mass density of the (non-porous) solid reactant. The specific internal energy on the adiabat is given for the polynomial (Eq. 3) by

$$\begin{aligned}\rho_0 e_{ad}(v_s) = A_1[V - \ln(V) - 1] + A_2\left[\frac{1}{V} - V + 2\ln(V)\right] \\ + A_3\left[V - \frac{3}{V} + \frac{1}{2V^2} - 3\ln(V) + \frac{3}{2}\right]\end{aligned} \tag{5}$$

where the relative volume, V, is

$$V = \rho_0 v_s \tag{6}$$

The Grüneisen coefficient is given by

$$\frac{\Gamma}{v_s} = \rho_0(B_0 + B_1\mu + B_2\mu^2) \tag{7}$$

The A-coefficients (Eq. 3) are fitted to available data for the reactant, either the measured Hugoniot of the unreacted solid, measured isotherms, or molecular dynamics calculations of the isotherms, together with an estimate of the Grüneisen parameter (B-coefficients, Eq. 7).

C. Equation of state of the skeleton/matrix

Matrix compaction is based on the P-α model described by (Herrmann 1969). The fundamental premise of that model is that if the solid equation of state has the form

$$P_s = f(v_s) \tag{8}$$

where P_s is the solid pressure (Eq. 1) and v_s is the solid specific volume, then the equation of state of the porous matrix has the form

$$P_m = f\left(\frac{v}{\alpha_H}\right) \tag{9}$$

where v is the total specific volume of solid plus void, and using the same functional dependence, f. Herrmann's distention ratio, α_H, was given by

$$\alpha_H = \frac{v}{v_s} \tag{10}$$

In his formulation, the mass fraction of gas product is always zero. In our generalization, we replace the specific volume of the mixture, v, (Eqs. 9 and 10) with the matrix specific volume, v_m.

$$v_m = \frac{v}{1-\lambda} \tag{11}$$

where λ is the mass fraction of gas product. The specific volume of the mixture, which is the reciprocal of the density, is the sum of gas and solid contributions,

$$v = \lambda v_g + (1-\lambda)v_s \tag{12}$$

where v_g is the gas specific volume. In what follows, we define our distention ratio, α, by

$$\alpha = \frac{v_m}{v_s} \tag{13}$$

With this change, the porosity, φ, which is the volume fraction of gas, Φ_g, is given by

$$\varphi = \Phi_g = \frac{\lambda v_g}{v} = \frac{v-(1-\lambda)v_s}{v} = 1 - \frac{v_s}{v_m} = 1 - \frac{1}{\alpha} \tag{14}$$

We modified Herrmann's implementation in three other ways. First, we assume that the unload-reload and crush curves are adiabats. In Herrmann's examples the reference curves were taken to be the normal Hugoniot of the solid. In other applications (Linde, *et al.* 1972) the reference curves were quasi-static (isothermal) unloading and crush curves. Second, we reduce the modulus for unloading-reloading by a multiplier, f_r, that is a linear function of our distension ratio.

$$f_r = f_{r1} + (1-f_{r1})\frac{\alpha_x - \alpha}{\alpha_x - 1}, \qquad \alpha \le \alpha_x \tag{15}$$

Here α_x is an input parameter, the maximum distention ratio that can support compressive stress. When the reactant is sufficiently dilute, the matrix relative volume exceeds a_x, and there is pressure equilibrium between the separated reactant particles and the gas product. For $\alpha > \alpha_x$, f_r takes the value f_{r1}. When α has the value 1, f_r takes the value 1. If the reactant is not dilute, so that the reactant particles touch, then the matrix carries some of the external load. Experimental models using dynamic photoelasticity illustrate the stress-bridging that can occur for the case where gas pressure is nil (Roessig and Foster 2001). In (Eq. 15) f_{r1} is the minimum ratio of the modulus of the porous solid to the modulus of the non-porous solid. In our work α_x is normally taken to be about 1.6 and f_{r1} is taken to be about 0.2. The unload-reload curve is then given by

$$P_{ur} = f_r P_{ad}\left(\frac{v_m}{\alpha}\right) \tag{16}$$

A reduction of the stiffness of the unload-reload curve with porosity is often observed experimentally. In addition, we found that calculations using a different porous crush algorithm (Reaugh 1987) exhibited reduced numerical noise when such a stiffness reduction was included. We use the solid reference adiabat (Eq. 3) as the basis function to calculate the unload-reload adiabat.

The matrix adiabat is the pressure per unit superficial area (solid plus gas volume). The matrix pressure is given by the same Grüneisen form as the solid (Eq. 1), and uses the same Grüneisen ratio (Eq. 7). The energy on the adiabat, however, is not amenable to an analytic form since the adiabatic pressure is path-dependent due to irreversible crushing. Instead, we perform a numerical integration for each element along its own path.

Next, the adiabatic pressure is assessed for tensile failure, using one of the three modules available in HERMES. (Tensile failure is described in Sec. III.A). If required, the stress tensor and porosity measures are adjusted. The crush curve, P_c, that limits the pressure for porous solids is then evaluated. In Herrmann's (and our) formulations the crush curve is a function of the distention ratio, and increases to a maximum as the distention ratio approaches 1.

$$P_c = g(\alpha) \tag{17}$$

We used one of Herrmann's example crush curves as a starting point. Ignoring the elastic limit, his curve is given by

$$P_c = P_0\left[1-\left(\frac{\alpha-1}{\alpha_x-1}\right)^{\frac{1}{c}}\right] \tag{18}$$

where in Herrmann's example, the power *c* is 2. Our third change is to modify the crush curve so that the crush pressure is achieved at a value of $\alpha_{\min}$ slightly larger than 1. (See Eq. 19). The purpose of this change is to permit the Newton iteration, we use to solve for the value of α on the crush curve at a given specific volume of the matrix, to achieve convergence, especially for c ≥ 4.

$$\begin{gathered} P_c = P_0\left[1+\delta_c-\left(\frac{\alpha-1}{\alpha_x-1}\right)^{\frac{1}{c}}\right] \\ \delta_c = \left(\frac{\alpha_{\min}-1}{\alpha_x-1}\right)^{\frac{1}{c}} \end{gathered} \tag{19}$$

With this change, the value of α where the pressure is zero, α_{max}, exceeds α_x.

$$\alpha_{max} = 1+(\alpha_x-1)(1+\delta_c)^c = \alpha_x+\delta_\alpha \tag{20}$$

If the unload-reload adiabat P_{ur} (Eq. 16) exceeds the crush pressure, the porosity is reduced so that the adiabatic pressure is equal to the crush pressure at the current specific volume of the matrix. Then the flow strength is calculated and the stress tensor evaluated for plastic flow (as described in Sec. III.B). If required, the stress tensor and porosity measures are adjusted. We illustrate the load-unload curves and the crush curve in Figure 2. The crush curve is shown as a solid line. It is assumed that the assembly started as poured, unconsolidated powder at initial relative volume 1.6, then loaded to various pressures, unloaded, and reloaded (dashed lines).

D. Calculation of pressure equilibrium

The equation for pressure equilibrium is based on multi-phase, multi-velocity formulations used for DDT (Baer and Nunziato 1986, Lapela *et al.* 2001) and for calculations of interior ballistics (Gough and Zwarts 1979). At pressure equilibrium, the solid pressure is given by

$$P_s = P_g + P_m/\Phi_s \tag{21}$$

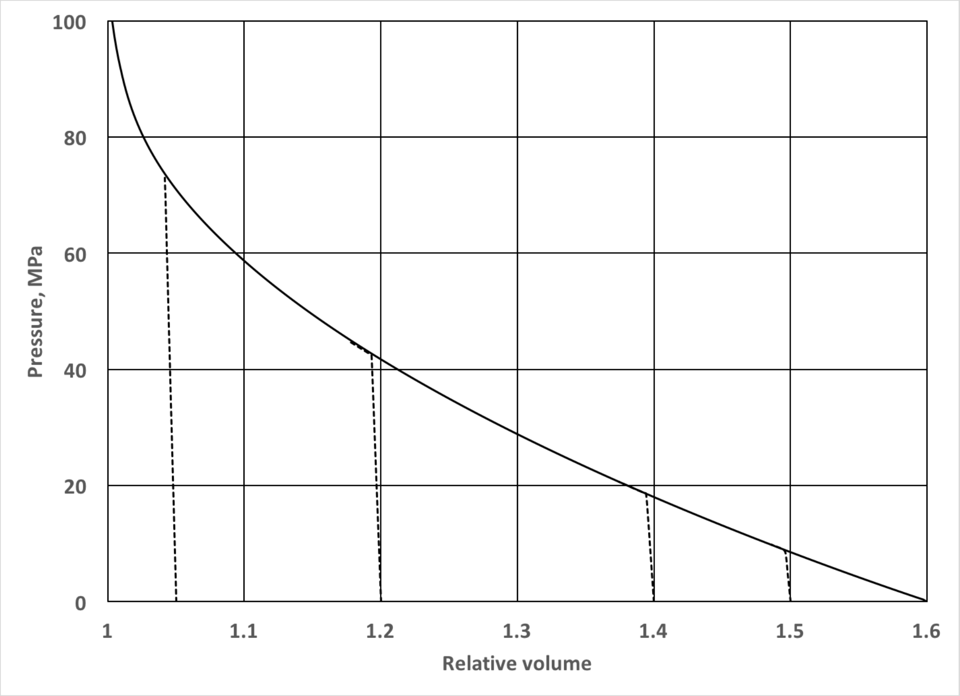

Figure 2. Crush curve (solid) from initial relative volume 1.6, loaded to various pressures and unloaded to various porosities (dashed curves) and reloaded. The crush pressure in this illustration is 100 MPa, and the power *c* has the value 2.

where P_m is the macroscopic matrix pressure, equal to the effective stress (Terzaghi *et al.* 1996, p89), exerted on the total cross section; Φ_s is the volume fraction of the reactant; and P_g is the pressure of the product gas. In this way, the solid pressure is the sum of the gas pressure and the pressure in the solid due to stress bridging. (Throughout, we assume that the volume fractions of each species and their area fractions are equal based on stereological principles.) If the porosity is so large that the solid particles are separated, the matrix contribution is nil, and the solid and gas pressures are equal. The total pressure of the mixture is given by

$$P = \Phi_g P_g + \Phi_s P_s = P_g + P_m \tag{22}$$

where

$$\Phi_g + \Phi_s = 1 \tag{23}$$

The matrix specific volume is given by (Eq. 11). It is unchanged by the partition of volume between the reactant and the gas product:

$$v_m = \frac{v}{1-\lambda} = \frac{\lambda}{1-\lambda} v_g + v_s \tag{24}$$

where v_s and v_g are the specific volumes of reactant and product. As a result, the macroscopic matrix pressure is unchanged during the iteration to pressure equilibrium. We note that (Eq. 23) is just (Eq.12) divided by v.

E. Energy partition during pressure equilibrium

For any volume element, conservation of energy in the absence of heat transfer is given by

$$de = -(P+Q)dv + dw_m \tag{25}$$

where e is the specific internal energy of the element, P is the element pressure, and Q is the artificial viscosity used in the computer simulation program to spread a shock front over a few computational cells. The term dw_m is the incremental work done against the stress-deviator tensor of the matrix.

$$dw_m = v_m(\tau_{xx}d\varepsilon_{xx} + \tau_{yy}d\varepsilon_{yy} + \tau_{zz}d\varepsilon_{zz} + \tau_{xy}d\varepsilon_{xy} + \tau_{yz}d\varepsilon_{yz} + \tau_{zx}d\varepsilon_{zx}) \tag{26}$$

where the total strain increments $d\varepsilon_{ij}$ are input to the model from the simulation program, and the stress-deviator tensor (τ_{ij}) is calculated in HERMES including strength effects (See Section III.B). In our formulation, the matrix is the only constituent that exhibits shear resistance.

The model must partition the energy among the constituents. For energy partitioning, we reject thermal equilibrium, which is an assumption that is inconsistent with the mesoscale picture of damaged explosive burning from exposed surfaces. We estimate the characteristic times for thermal and stress equilibrium by the following to show that stress equilibrium occurs much faster than thermal equilibrium.

Laminar burn speeds for the HMX explosives LX-10 and PBX 9501 are linear in pressure and were measured to be 200 mm/s at a pressure of 0.2 GPa (Tringe *et al*. 2014). Even for a fragment as small as 20 µm, the time to completely burn at that pressure is 50 µsec. The characteristic time for pressure equilibration in the same size fragment is 10 nsec, given by the ratio of the diameter to the sound speed in the solid, at least 2 mm/µs. In contrast, the time for thermal equilibrium from conduction is 250 µsec. As a consequence, the interior of the fragment is not preheated until the arrival of the burn front. Even for a detonation, described by the coalescence of burning hot spots, the product and reactant are separated by a flame thickness calculated to be 4 nanometers (Reaugh 2006). For a characteristic size of 2 µm the time to burn completely at 20 GPa is 50 nsec, but the characteristic time for thermal equilibrium is 700 nsec. The characteristic pressure equilibration time is 1 nsec.

As an alternative to thermal equilibrium, several authors have proposed (Cowperthwaite 1981, Partom 1981), or calculated (Reaugh and Lee 2002) the partition of energy during the transformation of reactant to product. These put the solid reactant on its adiabat and apply the left-over energy to the gas product. In addition, we need to partition the additional shock energy from the artificial viscosity, Q. We have chosen to add the shock energy to the solid when it can support bridging stresses. When the reactant is too dilute to support bridging stresses, the solid stays on its adiabat and the shock energy is added to the gas product. The closure for partitioning energy density among the constituents is

$$e = (1-\lambda)e_s + \lambda e_g \tag{27}$$

The incremental energy density of the solid is given by

$$de_s = -(P_m + Q)dv_m + dw_m - (P_s - P_m/\Phi_s)dv_s \tag{28}$$

and the gas is given the remaining energy density via (Eq. 27).

III. CALCULATION OF MECHANICAL FAILURE AND STRENGTH

In our model, shear strength and mechanical failure are associated with the matrix. If the porosity is so large that stress bridging does not occur, the shear strength is nil. (We neglect any viscous contribution of a particle-laden fluid.) The pressure dependence of shear strength uses the adiabatic matrix pressure, P_{adm}. In our calculation, the matrix pressure is first calculated assuming that the matrix is on the unload-reload path. The resulting stress tensor is tested for tensile failure (Sec. III.A) and adjusted as needed. The matrix pressure is then limited by the crush curve (Eq. 19) and the stress tensor evaluated for plastic flow (Sec. III.B).

A. Calculation of tensile failure

Tensile failure is accomplished using one of three mutually exclusive methods chosen by input parameters. The first (Sec. III.A. 1) is a limit on tensile pressure to avoid non-physical states of stress. It is not intended to have any mechanical significance or accuracy. The second (Sec. III.A.2) is intended to represent quasi-static or dynamic fracture toughness with a more-or-less mesh-independent formulation. In this module cracks are represented by adjoining mesh elements where the maximum principal stress (most tensile) is reduced to zero. The third (Sec. III.A.3) is intended to represent dynamic fragmentation including failure in both compression and tension. Each broken element carries a single fragment dimension, generally smaller than the element itself, and an associated porosity.

1. Minimum pressure module

The minimum pressure module, sometimes known as a "pmin" model, tests the unload matrix pressure including the Grüneisen energy dependence against an input parameter, P_{min}. If the unload pressure is more tensile than P_{min}, the pressure in that element is set to zero. When this happens, the element behaves as if it were a suddenly broken spring, and sends pressure waves (high-frequency noise) into neighboring elements. Since larger elements have more stored energy than smaller ones, the failure patterns developed by "pmin" models are notoriously mesh dependent.

2. Tensile fracture module

The tensile fracture module, implemented in HERMES, is intended to apply to individual cracks or a small network of interacting cracks. It was developed to replicate a model developed at LLNL, which is approximately independent of mesh size (Zywich 2013). Creating surface area is accompanied by irreversible energy absorption, which is tied to experimental fracture measurements. In this way, the element in question does not behave like a suddenly broken spring. Instead, energy is absorbed in creating fracture surfaces by gradually reducing the stress as a function of tensile strain. In the module, the energy absorbed when creating a given superficial surface area is made less dependent on mesh size by making the specific energy density absorbed proportional to the inverse mesh size.

The principal stress deviators, ordered so that the most tensile (largest algebraic value) is s_1, and the most compressive s_3, are given by the usual equations, for example (Fung and Tong, 2001, p88).

$$\begin{aligned}
\tau_0 &= \left(\frac{2}{3}J_2\right)^{1/2} \\
3\theta &= \cos^{-1}\left(\frac{\sqrt{2}J_3}{\tau_0^3}\right) \\
s_1 &= \tau_0\sqrt{2}\cos(\theta) \\
s_2 &= \tau_0\sqrt{2}\cos\left(\theta - \frac{2\pi}{3}\right) \\
s_3 &= \tau_0\sqrt{2}\cos\left(\theta + \frac{2\pi}{3}\right)
\end{aligned} \tag{29}$$

where J_2 and J_3 are the second and third invariants of the stress deviator tensor

$$\begin{aligned}
J_2 &= \frac{1}{2}\tau_{ij}\tau_{ij} \\
J_3 &= \frac{1}{3}\tau_{ij}\tau_{jk}\tau_{ki}
\end{aligned} \tag{30}$$

with the usual summation convention. It is not noted by Fung and Tong that the principal stress deviators, as given in (Eq. 26), are always ordered. That comes from the observation that the angle θ is between 0 and $\pi/3$, so $\cos(\theta)$ is between 0.5 and 1; $\cos(\theta-2\pi/3)$ between -0.5 and 0.5; and $\cos(\theta+2\pi/3)$ between -0.5 and -1.

The maximum principal stress on the matrix adiabat, $\sigma_1 = s_1 - P_{ad}$, is tested against the maximum permitted principal stress at failure, σ_{fail}

$$\sigma_{fail} = \sigma_{cr}\left(1 - d_f\right) \tag{31}$$

where σ_{cr} is a parameter, and d_f is the accumulated damage associated with tensile failure. If the value of σ_1 exceeds σ_{fail}, then the stress state, damage and porosity are updated. There are three cases to consider, according to (Zywich 2013).

a. The case where $s_1 = 0$ (all stress deviators 0)

The current volumetric strain, ε_v, and the nominal adiabatic matrix pressure, P^*_{adm}, is calculated

$$\begin{aligned}
\varepsilon_v &= -\left(\frac{1}{V} - 1\right) \\
P^*_{adm} &= K_f\varepsilon_v
\end{aligned} \tag{32}$$

where V is the updated relative volume, K_f is the unload reload modulus $f_r A_1$ (Eq. 3 and 16), and ε_v is positive in tension. We define the parameters ε_{cr} and ε_f by

$$\varepsilon_{cr} = \sigma_{cr}/K_f \qquad\qquad \varepsilon_f = \frac{2s\mathcal{G}}{\sigma_{cr}L} \tag{33}$$

where L is an input parameter corresponding to a characteristic dimension of the element, s is the ratio of hydrostatic to deviatoric fracture energy, taken to be 1/3, and $\mathcal{G}$ is the strain energy release rate (Zehnder 2012 p57), which is related to the plane-strain fracture toughness, K_{Ic}.

$$\mathcal{G} = \frac{K_{Ic}^2}{E}(1-\nu^2) \tag{34}$$

where E is Young's modulus and ν is Poisson's ratio.

The updated damage and matrix adiabatic pressure are calculated by the following replacements at each time step with the proviso that the damage does not decrease.

$$d_f \leftarrow \frac{\varepsilon_v - \varepsilon_{cr}}{\varepsilon_f - \varepsilon_{cr}} \qquad\qquad P_{adm} \leftarrow \frac{P_{adm}^* \varepsilon_{cr}(1-d_f)}{\varepsilon_{cr} + d_f(\varepsilon_f - \varepsilon_{cr})} \tag{35}$$

b. The case where P_{adm} is compressive and s_1 is tensile

The difference between σ_1 and σ_{fail} is used to calculate the damage increment.

$$\Delta d_f = \frac{(\sigma_1 - \sigma_{fail})A_T}{1 - \sigma_{cr}A_T} \tag{36}$$

where A_T is a parameter calculated from other input parameters

$$A_T = \frac{\sigma_{cr}L}{2\mathcal{G}(2G)} \tag{37}$$

where G is the shear modulus and L is the characteristic dimension of the element. The stress deviators are multiplied by a term S_{mul}

$$S_{mul} = \frac{1}{1 + 2G\Delta\lambda_f} \qquad\qquad \Delta\mathrm{\lambda_f} = \frac{\mathrm{\Delta d_f}}{\mathrm{2G(A_T s_1 - \Delta d_f)}} \tag{38}$$

The pressure P_{adm} is adjusted as in (Eq. 35).

c. The case where P_{adm} and s_1 are both tensile

This case is solved by a Newton iteration. A consistent new value of damage, d_f, is calculated so that the figure of merit, F_t, is nearly zero:

$$
\begin{aligned}
&P_{adm} = P^{*}_{adm}(1 - d_f) \\
&S_n = \sigma_{cr}(1 - d_f) \\
&S_{mul} = \frac{A_T S_n}{A_T S_n + \Delta d_f} \\
&F_t = S_{mul} s_1 - P_{adm} - S_n
\end{aligned}
\tag{39}
$$

The stress deviators are multiplied by the term S_{mul} and the pressure is updated as in (Eq. 35).

3. Fragmentation module

We wished to retain features of a fragmentation model we previously developed (Maienschein *et al.* 1998) to describe the impact fragmentation that would result from solid rocket motor fallback accidents. In its original form, the specific surface area, S/V, was given by

$$
\begin{aligned}
&\frac{S}{V} = A_s(\varepsilon - \varepsilon_0)\langle\dot{\varepsilon}\rangle, \text{for } \varepsilon > \varepsilon_0 \\
&\langle\dot{\varepsilon}\rangle = \frac{\int_0^t \dot{\varepsilon}^2 dt}{\int_0^t \dot{\varepsilon} dt}
\end{aligned}
\tag{40}
$$

where ε is the plastic strain. The parameter $\langle\dot{\varepsilon}\rangle$ is a measure of the average strain rate, but formulated so that it is unchanged after deformation stops. A_s and ε_0 are parameters. For our present application, we have introduced an additional input parameter S_{max}, so that the specific surface area is limited to that corresponding to a minimum fragment size, which we typically take as comparable to the explosive crystals used in the formulation. Until the plastic strain reaches the value ε_0, the specific surface area does not change. The use of the average strain rate was to permit extrapolation to linear scale factors spanning several orders of magnitude, in such a way that geometrically scaled experiments produced the same number of fragments. For our present purposes, the test experiments and the system-scale events to which the module will be applied do not differ by such a wide margin. As a result, we simplified the module by eliminating the strain-rate dependence.

$$
\frac{S}{V} = A_s(\varepsilon - \varepsilon_0), \;\; \varepsilon > \varepsilon_0 \tag{41}
$$

In contrast to the fallback application, however, the tests for which the module will be applied include both compressive and tensile loading. For that purpose, we have chosen to make ε_0 be smaller when the loading is largely tensile, and larger when the loading is compressive. We use the functional form we found suitable for describing ductile failure in metals (Wilkins *et al.* 1980):

$$
D_P = \int_0^{\varepsilon} w_p w_s d\varepsilon \tag{42}
$$

where the weighting function for shear, w_s, is taken to be unity, and the weighting function for pressure, w_p, is

$$
w_p = \frac{1}{1 + P_{adm}/p_0} \tag{43}
$$

where the pressure, P_{adm}, is positive in compression. As the tensile pressure approaches the negative of the positive input parameter p_0, the weighting function increases without bound. The parameter ε_0

is taken to be the value of plastic strain when the plastic damage variable, D_p reaches a critical input parameter value.

In our module, the porosity increases from fracture strain. To accomplish this, we introduce a tensile pressure limit, σ_{t0}, which decreases as an element's maximum porosity, ϕ_x, increases.

$$\sigma_{t0} = \sigma_0 \left(1 - \frac{\alpha_{mx} - 1}{\alpha_x + \delta_\alpha - 1}\right) \exp\left(-\frac{S}{V} L_0\right)$$
$$\alpha_{mx} = \frac{1}{1 - \varphi_x} \tag{44}$$

Here σ_0 and L_0 are input parameters. The reduction of the tensile pressure limit with fragment size (via S/V) is a way to account for the reduced ligament area of binder as the fragments get smaller. In most of our applications we have set L_0 to zero.

If the magnitude of the tensile pressure is calculated to be greater than σ_{t0}, the magnitude of the tensile pressure is reduced, and some of the volume strain is taken up as porosity. This is done in a gradual way, rather than suddenly reduced to zero, following the method of tensile fracture (Sec. III.A.2). When the tensile pressure first exceeds σ_{t0}, we save the value of α as the parameter α_l. We describe a damage value, D_t, which starts at zero, and increases to 1 when α increases from α_l to $\alpha_l + \varepsilon_f$. The input parameter ε_f is set so that creating a fracture surface with the same area requires the same energy, independent of the mesh size, Δx. For three-dimensional calculations with a fixed σ_{t0}, this requires ε_f to be proportional to $(\Delta x)^{-1}$. Following Zywich, we also assume it to be the case for two-dimensional axisymmetric calculations as well.

In our simplified module, we use only the tensile pressure, so that we can calculate the new damage, α, and pressure without iteration if the calculated tensile pressure exceeds $\sigma_{t0}(1-D_t)$ by the following replacement steps.

$$\varepsilon_t \leftarrow \frac{\sigma_{t0}}{K_f}$$
$$D_t \leftarrow \frac{1 - \varepsilon_t - \frac{\alpha_l}{V_m}}{\frac{\varepsilon_f}{V_m} - \varepsilon_t}$$
$$\alpha \leftarrow \alpha_l + D_t \varepsilon_f \tag{45}$$
$$P_{adm} \leftarrow -\sigma_{t0}(1 - D_t)$$
$$\varphi \leftarrow 1 - \frac{1}{\alpha}$$

where φ is porosity, V_m is the relative volume of the matrix, equal to $v_m \rho_0$, and K_f is the bulk modulus of the solid (Eq. 32).

Once the variable D_t reaches 1, (when the relative volume exceeds $\alpha_l + \varepsilon_f$), the tensile pressure is never permitted to exceed zero. If the magnitude of the unadjusted tensile pressure is calculated to exceed zero, then all the residual expansion from zero pressure is taken up as porosity, and α takes the value V_m. For this module, the element strength is multiplied by $(1-D_t)$.

B. Calculation of shear strength

In our model, we iterate on the plastic strain rate to achieve consistency with the strain-rate dependence of the shear strength.

1. Calculation of shear strength at a given plastic strain rate

Following (Vorobiev *et al.* 2007) the pressure- and strain- dependent strength is given by

$$Y_e = Y_i f_e(1-\Omega) + Y_r\Omega \tag{46}$$

where Ω is a damage measure that varies between zero and one, f_e is a strain hardening measure that has the maximum value of one, Y_i is the strength of the undamaged (intact) reactant, and Y_r is the (residual) strength of the fully damaged material. The damage parameter Ω, is given by

$$\Omega = \frac{D\ \max(0,\varphi\text{-}\varphi_{cr})}{1 + D\ \max(0,\varphi\text{-}\varphi_{cr})} \tag{47}$$

where φ is the porosity, and where D and φ_{cr} are parameters. The strain hardening term f_e is calculated by

$$f_e = \delta + C(1-\delta) \tag{48}$$

where C is a parameter between zero and one. The strain hardening measure δ, which varies between zero and one, is calculated by

$$\delta = \frac{\varepsilon_p}{\varepsilon_p + \varepsilon_h} \tag{49}$$

where ε_h is a parameter and ε_p is the plastic strain. The strength of fully damaged material (residual strength) is given by

$$Y_r = RY_0\left(\frac{A_r}{Y_0} + B_r\frac{P_m}{RY_0}\right) \tag{50}$$

where the parameter A_r is the cohesion, B_r is related to the friction angle, and Y_0 is the characteristic yield strength. P_m is the macroscopic matrix pressure. In this formulation, the pressure dependence of fully damaged material is not rate-dependent, but the pressure-independent part (cohesion) is rate-dependent. The residual strength is constrained not to exceed the intact strength. For geologic materials, the parameter A_r is taken to be zero for cohesionless soils and broken rock (Vorobiev *et al.* 2007). Here we let the parameter A_r be larger than zero to represent the observed rate-dependent residual strength of explosive at (nearly) zero pressure. The strain-rate parameter R is calculated by

$$R = \left(1 + \frac{\dot{\varepsilon}_p}{\dot{\varepsilon}_0}\right)^r \tag{51}$$

where $\dot{\varepsilon}_p$ is the plastic strain rate, and where r and $\dot{\varepsilon}_0$ are parameters.

The strength of the intact material also has a pressure dependence:

$$Y_i = RY_0 \left[\sqrt{o + m\frac{P_m}{RY_0} + (m/6)^2} - (m/6) \right], \qquad P_m \geq 0 \tag{52}$$

Here o and m are parameters and o generally takes the value one. For the case where $P_m < 0$, a straight-line interpolation between the uniaxial tensile strength, Y_t, and Y_i (0) is extrapolated to the pressure intercept at zero strength.

$$Y_i = Y_i(0) + \frac{3[Y_i(0) - Y_t]}{Y_t} P_m, \qquad P_m < 0 \tag{53}$$

where $Y_t = b_{ten} Y_0$, and the input parameter b_{ten} is the ratio of uniaxial tensile strength to uniaxial compressive strength. For metals, b_{ten} is about 1. For granular geologic materials, b_{ten} is typically 0.1. We note that (Eq. 51) (Vorobiev *et al*. 2007) has the disadvantage of being unbounded at high strain rates. The experimental data typically available from Split Hopkinson Pressure Bar apparatus (SHPB) are limited to a strain rate of a few thousand per second. Dynamic tests, even at velocity < 30 m/s can lead to local strain rates more than ten times the SHPB limit. In plane shocks, the strain rates are a few hundred times that limit. As a result, the extrapolated rate-dependent strength can become larger than is plausible. We incorporated a strength limiter that is applied smoothly, rather than an abrupt cut-off. The nominal strength Y_e (Eq. 46) is scaled to an input parameter Y_{max}. That maximum value is applied for all values of Y_e, so must be included when fitting parameters to experimental data:

$$Y = Y_{max} \frac{Y_e/Y_{max}}{1 + Y_e/Y_{max}} \tag{54}$$

2. Iteration of strength to convergence on strain rate

The section above describes the calculation of the yield strength as a function of an assumed plastic strain rate. We perform an iteration on yield strength to converge to a strain rate using the figure of merit, F_y:

$$F_y = 3G\dot{\varepsilon}_p \Delta t + Y - \tilde{\sigma} \tag{55}$$

where G is the shear modulus, Δt the time step, and $\tilde{\sigma}$ the equivalent stress assuming the stress tensor were incremented elastically. We found that the change in slope of the yield stress near zero pressure was enough to prevent convergence with a Newton method solver. Instead we have implemented a robust but slow solver that logarithmically bisects the highest and lowest strain rates to find the subsequent trial value. The initial limits are between 0 and, $\dot{\varepsilon}_{max}$where

$$\dot{\varepsilon}_{max} = \frac{\tilde{\sigma}}{3G\Delta t} \tag{56}$$

If the plastic strain rate is zero, the strength takes its minimum value, and the elastic assumption for $\tilde{\sigma}$ was correct. The upper limit to plastic strain rate is if all the applied strain increment is plastic, which results in the largest possible strength for this element at this time. Convergence is achieved when the value of the figure of merit is less than an input tolerance (we typically use values between 10^{-7} and 10^{-5}) multiplied by a characteristic value of the strength, Y_0.

3. Calculation of the increase in porosity

The increase in porosity (dilatency) common to granular geologic materials and assumed to be present in granular energetic materials, is calculated by

$$\dot{\varphi} = A\frac{dY}{dP_m}\dot{\varepsilon}_p(1-\varphi) \tag{57}$$

(Vorobiev *et al.* 2007) and is thermodynamically stable when the parameter A < 1. In our case, we use

$$A = \frac{A_0 + A_1\dfrac{dY}{dP_m}}{1+\dfrac{dY}{dP_m}} \tag{58}$$

where both A_0 and A_1 are taken to be less than 1. With the relatively simple analytic expressions for the pressure dependence of the intact and broken solid (Eq. 50, 52-54), we use analytic derivatives.

4. Calculation of the Mohr-Coulomb yield surface

For metals and clays, the von Mises yield surface for strength is widely used. In principal stress space, with axes (σ_1, σ_2, σ_3), the von Mises yield surface is a circular cylinder whose axis is the principal diagonal in the (1, 1, 1) direction. A cross-section normal to that cylinder (at constant pressure) is a circle, whose radius is the equivalent stress. See Fig. 2. The equivalent stress is given by $\sqrt{3J_2}$. Although experiments to probe the yield surface are difficult, they have been done in a few instances, and for metals and clays, the yield surface can be nearly circular. Some tests with an aluminum alloy (Wilkins *et al.* 1980) have shown that even for metals, the equivalent strength in shear may not lie on the circle scaled to compression or tension. We are ignoring here such effects as kinematic hardening, whereby the circle does not expand with increasing plastic strain, but rather translates in the direction of straining.

In contrast, for geologic and dry granular materials, the Mohr-Coulomb criterion is widely used (Fung and Tong, 2001 p161-163). (HERMES includes an input parameter to select the Mohr-Coulomb criterion.) The condition for that criterion is

$$\frac{\sigma_c - \sigma_t}{2} = f_1\left(\frac{\sigma_c + \sigma_t}{2}\right) \tag{59}$$

where σ_c is the most compressive principal stress and σ_t is the most tensile principal stress. The dependence is the arbitrary function f_1. In this formulation, compressive stresses are positive. Most hydrodynamics codes follow the convention (Wilkins 1999) that the principal stresses and stress deviators are positive in tension, and pressure is positive in compression. In terms of the principal stress deviators ordered algebraically,

$$s_1 \geq s_2 \geq s_3 \tag{60}$$

the Mohr-Coulomb criterion is rewritten for that convention as

$$\frac{s_1 - s_3}{2} = A_{mc} + B_{mc}\left(P_m - \frac{s_1 + s_3}{2}\right) \tag{61}$$

where we have made the general functional dependence a (locally) linear one.

For our explosive, the data for pressure, strain-, and strain-rate dependent flow strength were taken in either uniaxial or triaxial compression. In uniaxial compression, the lateral stress is zero, whereas in triaxial compression, the lateral stress is compressive. In either case, two of the three principal stresses are equal and less compressive than the third (axial) component. It is therefore convenient to make the basis for the module the equivalent stress in compression, so that

$$Y_c = f_2(P_m) \tag{62}$$

where we use f_2 to represent the pressure dependence described above in sections III.B.1 and 2. It is convenient to express other states of stress by the parameter ξ where

$$\begin{aligned} s_2 &= \xi s_1 \\ s_1 + s_2 + s_3 &= 0 \end{aligned} \tag{63}$$

Since we use the radial return method (Wilkins 1999) for reducing the stress tensor from the elastic trial state to the yield surface, the parameter, ξ can be evaluated from the elastic trial state before the flow stress is calculated. For uniaxial compression, $\xi = 1$. For uniaxial tension, $\xi = -1/2$. In shear, $\xi = 0$. In uniaxial compression, (Eq. 61) can be written

$$\frac{3s_1}{2} = A_{mc} + B_{mc}(P_m + s_1/2) \tag{64}$$

We then evaluate the yield stress in compression as

$$Y_c = \sqrt{3(s_1^2 + s_2^2 + s_3^2)/2} \tag{65}$$

so that (Eq. 64) becomes

$$Y_c/2 = A_{mc} + B_{mc}(P_m + Y_c/6) \tag{66}$$

We evaluate B_{mc} from (Eq. 66) by calculating the tangent to the yield surface (Eq. 62).

$$B_{mc} = \frac{f_2'}{2 + f_2'/3} \tag{67}$$

where $f_2^{'}$ is the pressure derivative of f_2. At present, we are using an approximate function, $A_r \exp(-P_m/Y_0)$ to calculate the pressure derivative. We found that the discontinuous change in the pressure derivative near to where the residual strength is limited to be no larger than the intact strength led to a discontinuous change in the slope, B_{mc}, and a discontinuous change to the calculated strength. This prevented convergence. A more satisfactory solution would be to force the residual strength to approach the intact strength gradually as a function of pressure. This has not yet been implemented.

We evaluate (Eq. 61) for the general value of ξ to obtain

$$(1 + \xi/2)s_1 = A_{mc} + B_{mc}P_m + B_{mc}\xi s_1/2 \tag{68}$$

We use (Eq. 66) to evaluate (A_{mc}+$B_{mc}P_m$) in terms of Y_c, and note that

$$Y_\xi = \sqrt{3(1 + \xi + \xi^2)s_1^2} \tag{69}$$

In terms of the compressive yield stress,

$$Y_\xi = \frac{\sqrt{3(1 + \xi + \xi^2)}(1 - B_{mc}/3)}{2 + (1 - B_{mc})\xi} Y_c \tag{70}$$

The intersection of the yield surface with the plane perpendicular to the main diagonal or pressure axis, $\sigma_1 = \sigma_2 = \sigma_3$, is shown in Fig. 2 for three values of f_2'. The extreme value of three is the largest possible value, and corresponds to a friction angle of 90° where B_{mc} takes the value one. The slope of one ($B_{mc} = 0.43$) is typical of rocks and soils. The value zero corresponds to no pressure dependence, and for that case the yield surface is equivalent to the Tresca condition (Fung and Tong 2001 p158). The importance for our work is that the equivalent strength in pure shear is reduced relative to that in compression from 0.866 for no pressure dependence to 0.577 for the pressure derivative equal to three. A modification of the triax test might be used to determine the suitability of the Mohr Coulomb model. After the application of isostatic stress, the axial load could be reduced, rather than increased. This loading path is triaxial "tension" although all principal stresses are compressive. In Fig. 2, triaxial tension obtains on the corners of the yield surface that (apparently) intercept the three principal stress axes. The calculated and measured strengths could then be compared at several different confining pressures.

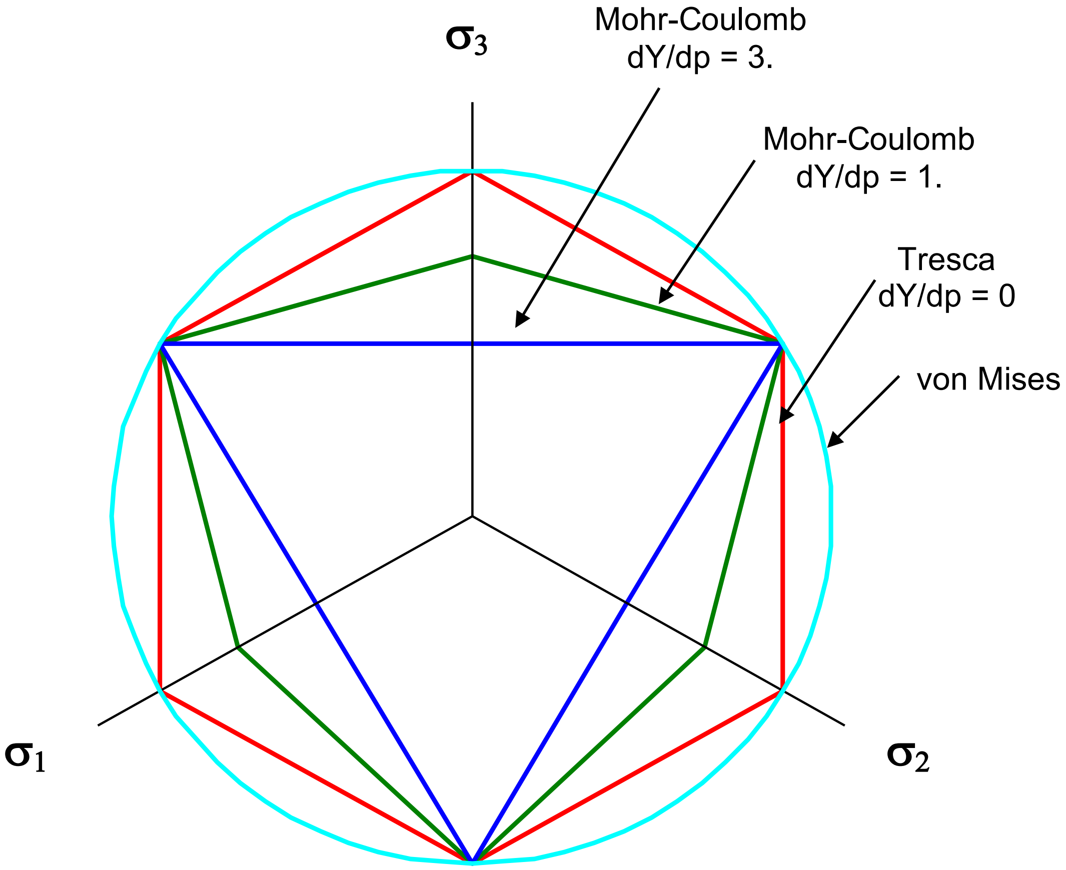

Figure 2. Intersection of the yield surface with a plane normal to the pressure axis. All surfaces are normalized to have the same value in triaxial compression. The three axes (thin black lines) are the three principal stresses. In this figure, the principal stresses are not ordered.

IV. CALCULATION OF THE CHANGE IN COMPOSITION (BURN)

An important capability of the HERMES model is to quantify the amount of reactant that is converted to gas product as a function of time. The reaction violence of the event depends on both the amount of product and the time over which it is formed. For a given violence metric there is an associated characteristic time. If the product mass is developed more quickly than that, the violence measure is about the same as that produced by a detonation of the same mass of explosive. If the time to burn takes much longer than that, the violence measure is much reduced over that produced by a detonation. We quantified this effect when air blast is used as the violence measure (Reaugh *et al.* 2012). A similar effect, although with different characteristic times, also holds for the response of the surrounding confinement, whether measured by crater volume or shrapnel velocity.

In HERMES, there are separate modules that describe ignition from a mechanical insult that does not produce shocks, the propagation of an ignition front through a mass of damaged material, the subsequent burning of the material, and the growth of reaction to detonation if strong shocks develop. In our formulation, the post-shear-ignition burning and the post-shock-initiation burning occur simultaneously. Both contribute to the evolving mass of product gas.

A. Calculation of ignition without shocks

The basis of our shear-ignition criterion is the observation that in low-speed impacts, ignition is accompanied by significant shear deformation. We do not identify whether the localization mechanism is crystal twinning, continuum shear bands, friction, or grain-to-grain slip. Instead, we use properties of the stress tensor to identify where shear deformation dominates.

The ignition parameter is an integral over plastic strain but with weighting factors for shear deformation and for the normal stress acting on the plane of maximum shear. When the normal stress is tensile, the weight is zero. This factor was motivated by the view that more frictional work is done on an interface when the normal stress is more compressive. The ignition parameter is given by

$$D_{\text{ignit}} = \int_0^t f_\tau f_\sigma \dot{\varepsilon}_p dt \tag{71}$$

where the shear weighting factor, f_τ , is given by

$$f_\tau = \left(2 - \frac{27|J_3|}{2Y^3}\right)^\tau \tag{72}$$

where Y is the equivalent stress, $\sqrt{3J_2}$. The weighting term inside the parentheses (Eq. 72) has the value 2 in shear and the value 1 in compression or tension. When the factor is raised to a power, τ, approximately 4, there is an order of magnitude difference for the weight during shear deformation than for compression or tension. The normal stress weighting factor, f_σ is given by

$$f_\sigma = \left(\frac{P_m + s_2/2}{\sigma_0}\right)^{1/2} \tag{73}$$

Here σ_0 is a parameter of order 50 MPa. Use of this criterion in simulations of the US and UK variants of the Steven test (Reaugh and Jones 2010) has shown that ignition in both tests occurs when D_{ignit} reached the same value, although the peak pressures in the two tests differ by nearly a factor of two. Similarly, scorch marks on the steel holder from UK tests are not on the axis of symmetry, where the pressure is largest, but at an intermediate radius, near where our ignition criterion has its maximum value (Curtis, *et al.* 2012). Computer simulations of those tests have shown that the value of the ignition criterion is quite sensitive to the coefficient of friction used. A separate parameter study, using a simplified geometry where a disk of explosive is crushed between two platens, illustrated both the sensitivity to friction, and how the localization of plastic strain depends on the pressure- and strain-rate- sensitivity of the flow stress (Reaugh, 2010). If the flow stress is assumed constant, the maximum strain developed, and the maximum value of the ignition criterion, is inversely proportional to the mesh size. With pressure- strain- and strain-rate dependence as given in Sec. III.B.1 and 2, the ignition criterion decays exponentially with increasing distance from the surface – the e-folding length for one explosive was about 0.6 mm (Reaugh and Jones, 2010). This result is analogous to the development of a boundary layer in gas dynamics, where the characteristic thickness of the layer is determined by the flow velocity and the viscosity, a particular instance of rate-dependent shear strength.

B. Calculation of sub-sonic burning after ignition

Once an element is ignited, it is assumed to burn as an assembly of particulates with a starting specific surface area. For smooth, compact objects the specific surface area is simply related to the characteristic dimension, D_c.

$$\frac{S}{V} = \frac{6}{D_c} \tag{74}$$

For spheres, D_c is the diameter. For cubes, D_c is the length of an edge. For naturally broken material, the specific surface area will be larger than that implied by its nominal size. However, the value depends on the scale of the irregularity that is resolved by the measurement technique.

For our purposes, the scale of irregularity is determined by the scale that can be sensed by an advancing flame. The frangibility test (shotgun test) (Atwood, *et al.* 2007) has been used to characterize propellant or explosive response to mechanical insult. In that test, an explosive or propellant sample is impacted on a steel plate. The resulting fragments are collected and burned in a closed bomb, and the pressure history measured. Results of that test can be used to determine the specific surface area as a function of impact velocity, typically in the range 30 to 300 m/s (Maienschein et al. 1998).

The rate of change of the mass fraction converted to product for fragments burning from their surface inward is given by

$$\dot{\lambda} = \frac{S}{V} v_b(P)(1-\lambda)^{2/3} \tag{75}$$

where v_b is the pressure-dependent laminar burn speed. Here S/V is the specific surface area before burning starts. At a given pressure, the mass burning rate of broken material is larger than that measured for intact material. The ratio of the burning rates is the ratio of the surface areas. One complication in interpreting the test results is that fragmentation of the propellant or explosive is not uniform throughout the damaged volume. The pile of resulting fragments has a broad size distribution. We were, however, able to determine parameters for a simple linear dependence of specific surface area with plastic strain (Maienschein *et al.* 1998). If the fragmentation model is not operative, we use (Eq. 41) to calculate the surface area but with the critical plastic strain taken to be ε_0 an input parameter. We have chosen "reasonable" values for the two parameters when data are absent. There are limited data available for specific formulations. In principle, frangibility tests can be performed on explosives, and in practice they are sometimes tested. In general, explosives are more difficult to ignite than propellants so that the early pressure history recorded in these tests can be affected by the increased amount of ignition aid needed to start the fragments burning. Recent observations of quasi-static damage (Wiegand, *et al.* 2011) suggest that high confining pressure may significantly reduce the surface area developed with plastic strain. The fragmentation module (Sec. III.A.3) includes the capability for reproducing such data.

C. Calculation of the spread of an ignition front

The permeation of hot product gas through a damaged reactant bed depends on the viscosity of the hot gas, the local channel dimension, and the local pressure gradient. Once hot gas arrives at the surface of cooler reactant, there is an induction time, which depends on the thermal properties of the reactant and the chemical kinetic reaction rates, before a self-sustaining local flame can start. This is an active research area for experiments and for multi-velocity, multi-phase computer simulations. Direct numerical simulation at the mesoscale, resolving both the boundary layer of flow through a channel, heat transfer between the hot gas and the solid, and the growth of reaction from a (reduced) chemical reaction net could be a fruitful and complementary approach. So far as we know, this has not yet been attempted.

In HERMES, we have taken the simplification of using an input value for the ignition front velocity, which probably should depend on the local pressure and porosity. We anticipate that the results of research would be used to calculate the local time of ignition more adequately. In the interim, we have performed a limited number of parameter studies that show the ignition front velocity can have a significant effect on the subsequent response (Reaugh *et al.* 2014). Other computer simulations with a much smaller sample volume showed less effect of ignition front velocity. In those latter simulations, most of the porous bed had ignited before significant deformation occurred.

D. Calculation of the growth to detonation

If broken, porous explosive is shocked with sufficient amplitude, a detonation can develop. It is observed for all explosives that for one-dimensional plane shocks, the distance between the surface where a shock was introduced, and the point in the interior of the explosive where detonation develops (run-distance), depends on the shock amplitude. Weaker shocks require a longer run-distance to develop. Detonation models reproduce this feature. In addition, the CREST model distinguishes shocks from gradual pressure rises. We have chosen a simple subset of the CREST equations to couple detonation development with the growth of reaction due to burning in broken material. The subset of the CREST reaction model we use is given by

$$
\begin{aligned}
&\dot{\lambda} = m_2\dot{\lambda}_2(1-\lambda) \\
&\dot{\lambda}_1 = (1-\lambda_1)\sqrt{(-2b_1\ln(1-\lambda_1))} \\
&\dot{\lambda}_2 = \lambda_1(1-\lambda_2)\sqrt{2b_2\left[\frac{b_2\lambda_1}{b_1}-\ln(1-\lambda_2)\right]} \\
&b_1 = c_0(Z-c_{13})^{c1} \\
&b_2 = c_2(Z-c_{13})^{c3} \\
&m_2 = \frac{c_{10}}{\sqrt{b_2}}(Z-c_{13})^{c11}
\end{aligned}
\qquad (76)
$$

Here we have retained the notation of (Handley 2011). The variable λ is the mass fraction of product gas, and the superior dot signifies the time-derivative. The *Z* parameter is a function of entropy as described by (Lambourn, 2006). The c_i parameters are input values. The parameter c_{13} may be positive, negative, or zero. The resulting pop plots (run distance as a function of shock pressure) exhibit either a cut-off shock pressure (below which a detonation does not form) when c_{13} positive, or an asymptotic run distance approached at low shock pressure when c_{13} negative, or an approximate power-law dependence when c_{13} is zero.

The *Z* parameter as used in the original CREST model does not consider either plastic work in shear or the plastic work of irreversible compaction. Those applications to detonation have ignored both strength in the reactant and resistance to compaction (they use a snowplow approximation) as being small compared with detonation shocks. In our work, which applies both to shocks and modest deformations, we only consider the irreversible work associated with shocks (Q-heating), and subtract the plastic work from the energy density to calculate *Z*. We also we subtract the irreversible adiabatic energy of compaction, unload and reload.

We found that we could interpolate the shock-sensitivity of explosives as a function of porosity by using an analytic modification to (Eq. 76). The input parameters c_0, c_2, and c_{10} are multiplied by a power of F_c, which is a function of porosity. Data for shock sensitivity of explosives as a function of porosity is generally sparse. We have fitted experiments on HMX-based explosives and double-base propellants with the function

$$\begin{aligned} &F_c(\phi) = \exp\left(-\frac{\phi_m}{A_c + B_c\phi_m}\right) \\ &c_0' = c_0 F_c^{c1} \\ &c_2' = c_2 F_c^{c3} \\ &c_{10}' = c_{10} F_c^{c11} \end{aligned} \tag{77}$$

where ϕ_m is the porosity caused by mechanical effects, but not by burning. A_c and B_c are input parameters. Since F_c is less than one, a given value of *Z* is less efficient at producing the reaction rate for porous explosives.

V. APPLICATIONS OF THE HERMES MODEL

A. Shear Ignition

During the development of HERMES, we have published results of our applications to laboratory-scale experimental test configurations. In (Reaugh and Jones 2010) we fitted the strength model to results of mechanical property tests on a UK HMX-based explosive, and applied the shear ignition module to evaluate the ignition parameter in two variants of the Steven test (Chidester *et al.* 1992). We found that the same value of the ignition parameter occurred at the experimental “go/no-go” threshold velocities (70 m/s for the UK variant and 110 m/s for the US variant). The calculated peak pressures in these tests (1.4 GPa for the UK variant and 0.9 GPa for the US variant) differ because the fixture support for the two variants are quite different. The calculated location of the maximum value of the ignition parameter was adjacent to the back plate in a ring that surrounds the center of impact. In (Curtis *et al.* 2012) a photograph of a recovered UK fixture for a “go” showed a discolored ring surrounding the center of impact.

Application to the spigot intrusion test (Hughes *et al.* 2012) and (Hughes *et al.* 2014) were less successful. In those applications, HERMES was used in the finite element program LS-DYNA (Hallquist, 1998), which we used in a Lagrange framework, as were the applications to the Steven test above. However, the severe mesh distortion near the spigot as it punches through the explosive stopped this calculation early. Subsequent tests with HERMES in ALE-3D (Noble *et al.* 2017) were more successful when using an Eulerian or Arbitrary Lagrange Eulerian (ALE) framework. These test calculations have not been published.

Applications to shear localization in an idealized drop test (Curtis and Reaugh 2016) were successfully carried out through ignition and early post-ignition burning in a Lagrange formulation. Simulations of the skid test (White *et al.* 2014) compared with experiment showed the ignition parameter to have a much-reduced value compared to Steven test results at drop conditions corresponding to an experimental “go”. The inference drawn there was that the well-understood influence of high melting-temperature grit on the surface was the cause. However, experiments with gritted Steven tests have not been performed, and skid test experiments on clean surfaces produced no ignition (Heatwole *et al.* 2015). As a result, there is no quantitative change to shear ignition sensitivity caused by the presence of grit that can be demonstrated.

B. Deflagration-to-Detonation Transition (DDT)

Applications to DDT have calculated the response of porous explosives in an experimental test fixture. (Reaugh et al. 2014) performed simulations of LX-04 (85% HMX, 15% Viton binder) molding powder beads confined in a thick-walled steel tube. At that time, the all-porosity variant of CREST was not available so the DDT calculation was performed at 15% porosity, and the CREST detonation parameters were fitted to SDT experiments on 15% porous HMX Class 1 powder. There were no DDT experiments performed at that porosity, but the calculated transition distance was consistent with the measured transition distance as a function of porosity.

A subsequent application to 180 μm PETN powder at 21% porosity had the advantage of both SDT tests and DDT tests at the same porosity. The speed of the ignition front through that powder, and the particle size distribution around the 180 μm mean value were not measured, and the calculations (Reaugh et al. 2018) showed the sensitivity of the calculated transition distance to estimated value ranges of those parameters. The calculations also demonstrated the processes leading to DDT. The burning explosive creates a plug of higher-density powder that moves into the undisturbed powder as a weak shock. In the calculations, the build-up to detonation starts just behind the shock front. This phenomenon has been measured in SDT experiments instrumented with either pressure or velocity gauges. Other calculations addressed the DDT transition of HMX Class 1 powder in Lexan tubes (Tringe *et al.* 2017) whose experimental diagnostics included visible light and flash X-ray diagnostics.

C. Future Applications

We will apply the all-porosity CREST model to calculations of the DDT transition distance as a function of porosity. It is possible that the PETN experiments (Luebcke et al. 1996) would be suitable candidates, because SDT tests have been performed at several porosities.

The fragmentation and all-porosity SDT model were developed to enable calculations of XDT. Although we have performed a few initial calculations, we have not yet systematically applied the model to the wide variety of test configurations in the literature that have led to XDT.

The ALE framework makes it possible to examine the post-ignition spread of reaction and subsequent reaction violence in both laboratory tests and postulated accidents. This aspect has only begun to be explored.

VI. ASSESSMENT

At the present, the HERMES model can calculate the mechanical and energetic response of explosives and propellants to mechanical stimulus. Until recently, there have been just a few of us who have exercised the model, and that has been for a limited number of examples. We have recently added a few additional users. As is always the case, they have uncovered errors which we have subsequently fixed. As a result, the model has been made more robust, in that no changes have been required to continue or complete the calculations.

The spirit of our development has been keep the various modules as simple as we could, and still represent the phenomena we know (or suspected) to have importance in the response. In some cases, the modules are too simple. In other cases, they may well be not simple enough. The module for strength is about as simple as is consistent with describing a material that exhibits pressure, strain, and strain-rate dependent hardening that varies with the initial temperature. The various parameters of the model are difficult to fit to experiment because of their non-linear interactions with each other. Our module for the propagation of a flame front in lightly or heavily damaged material (an input constant) is too simple, but experiments have not produced unambiguous results.

Because we iterate pressure equilibration to convergence and a separately iterate strength to convergence, HERMES can be up to 10 times slower than standard equations of state and strength. This puts a burden on load balancing for parallel processing. In Lagrange simulations, the HERMES material stays with the elements that it starts in, so that load balancing can be straightforward. In Eulerian simulations, the post-ignition HERMES material eventually spreads throughout the mesh, which would require a relatively sophisticated load-balancing algorithm.

Nevertheless, we are satisfied that we have a computational model that can be used as computational models have traditionally been used. We perform computations with the model to help understand the results of the last set of experiments, and then perform computations with the model to help design the next set of experiments.

ACKNOWLEDGMENTS

The HERMES model described here was begun during a two-year secondment of JER at AWE. Continued development of the model was fostered by an on-going collaboration that has included additional secondments of JER at AWE and of JPC at LLNL. It has been sponsored and encouraged by a number of on-going programs at both laboratories; JER, BWW and HKS have been funded in part by the Joint US DoD/DOE Munitions Technology Development Program.

Lawrence Livermore National Laboratory is operated by Lawrence Livermore National Security, LLC, for the U.S. Department of Energy, National Nuclear Security Administration under Contract DE-AC52-07NA27344.

REFERENCES

Atwood, A. I., K. P. Ford, D. T. Bui, P. O. Curran, and T. M. Lule, "Assessment of mechanically induced damage in solid energetic materials*,"* 7th *Int. Symposium on Special Topics in Chemical Propulsion*, Kyoto, Japan, September 2007.

Baer, M. R. and J.W. Nunziato, "A two-phase mixture theory for the deflagration-to-detonation transition (DDT) in reactive granular materials," *Int. J. Multiphase Flow*, **12** (6) p861-889, 1986.

Bastea, S., K. Glaesmann, and L.E. Fried, "Equations of state for high explosive detonation products with explicit polar and ionic species," *Proceedings, 13th International Detonation Symposium*, Norfolk, VA, July 2006, p1137.

Chidester, S. K., L. G. Green, and C. G. Lee, "A Frictional Work Predictive Method for the Initiation of Solid High Explosives from Low-pressure Impacts," *Proceedings, 10th International Detonation Symposium*, Boston, MA, July 1993, p786

Cowperthwaite, M. "A constitutive model for calculating chemical energy release rates from the flow fields in shocked explosives", *Proceedings,7th Symposium (International) on Detonation, Annapolis, MD, June 1981*

Curtis, J. P., A. G. Jones, C. T. Hughes, and J. E. Reaugh, "Modelling violent reaction following low speed impact on confined explosives," *Proceedings of the 7th Biennial Conference of the American Physical Society Topical Group on Shock Compression of Condensed Matter*, Chicago, IL, AIP Conference Proceedings Volume **1426**, 2012, p669.

Curtis, J. P. and J. E. Reaugh, "Modelling the Ignition of Explosives by Pinch with the HERMES Model, *Procedings, 42nd International Pyrotechnics Symposium*, Grand Junction, CO, 2016 pnnn.

Fried, L. E., W.M. Howard, and P.C. Souers, "EXP6: A new equation of state library for high-pressure thermochemistry," *Proceedings, 12th International Detonation Symposium*, San Diego, CA, August 2002.

Fung, Y. C. and P. Tong, *Classical and Computational Solid Mechanics*, World Scientific, Singapore, 2001.

Gough, P. A., and F.J. Zwarts, "Modeling Heterogeneous Two-Phase Reacting Flow," *AIAA Journal*, **17** (1) Jan. 1979, p17.

Hallquist, J. (Compiler) *LS-DYNA Theoretical Manual*, Livermore Software Technology Company Report, Livermore CA, Mau 1998.

Handley, C. A. "The CREST Reactive Burn Model, *Proceedings, 13th International Detonation Symposium*, Norfolk, VA, July, 2006, p864.

Heatwole, E., G. Parker, M. Holmes, P. Dickson, "Grit-mediated frictional ignition of a polymer-bonded explosive during oblique impacts: Probability calculations for safety engineering," *Reliability Engineering and System Safety,* **134**, p10 (2015).

Herrmann, W., "Constitutive Equation for the Dynamic Compaction of Ductile Porous Materials," *J. Appl. Phys.*, **40** (6) May, 1969, p2490.

Hughes, C. T., J. P. Curtis J. E. Reaugh, A. G. Jones, "Explosive Response to Low-Speed Spigot Impact," *Proceedings, 38th International Pyrotechnics Symposium*, Denver, CO, 2012 p338.

Hughes, C. T., J. P. Curtis, J. E. Reaugh, and A. G. Jones, "Explosive Response to Pinch Arising from Low Speed Spigot Impact, *Proceedings, 15th International Detonation Symposium*, San Francisco, CA, July 2014, p683.

Lambourn, B. D., "A complete EOS for non-reacted explosives," *Proceedings of the Conference of the American Physical Society Topical Group on Shock Compression of Condensed Matter*, Baltimore, MD, AIP Conference Proceedings Volume 845, 2006, p165.

Lapela, A. K., R. Menikoff, J.D. Bdzil, S.F. Son, and D.S. Stewart, "Two-phase modeling of deflagration-to-detonation transition in granular materials: Reduced equations," *Physics of Fluids*, **13** (10) p3002-3024, October 2001.

Linde, R. K., L. Seaman, and D.N. Schmidt, "Shock response of porous copper, iron, tungsten, and polyurethane," *J. Appl. Phys.*, **43**, (8) 1972, p3367.

Luebcke, P. E., P. M. Dickson, J. E. Field, "Deflagration-to-detonation transition in granular pentaerythritol tetranitrate,", *J. Appl. Phys.* **79** (1996) p3449.

Maienschein, J. L., J. E. Reaugh, and E. L. Lee, *Propellant Impact Risk Assessment Team Report: PERMS Model to Describe Propellant Energetic Response to Mechanical Stimuli*, UCRL-ID-130077, February 27, 1998.

Noble, C., A. Anderson, N. Barton, J. Bramwell, A. Capps, M. Chang, J. Chou, D. Dawson, E. Diana, T. Dunn, D. Faux, A. Fisher, P. Greene, I. Heonz, Y. Kanarska, S. Khairallan, B. Liu, J. Margraf, A. Nichols, R. Nourgaliev, M. Puso, J. Reus, P. Robinson, A. Shestakov, J. Solberg, D. Taller, P. Tsuji, C. White, and J. White, *ALE3D: An Arbitrary Lagrangian-Eulerian Multi-Physics Code*, Lawrence Livermore National Laboratory report, LLNL-TR-732040, May 2017.

Partom, Y. "A void collapse model for shock initiation," *Proceedings,7th Symposium (International) on Detonation, Anapolis, MD,* June 1981, p 506

Reaugh, J. E., "Computer Simulations to study the explosive consolidation of powders into rods*,"* *J. Appl. Phys.*, **61** (3) 1987, p962.

Reaugh, J. E., "Multi-scale computer simulations to study the reaction zone of solid explosives," *Proceedings, 13th International Detonation Symposium*, Norfolk, VA, July 2006, p1276.

Reaugh, J. E., "*Modifications and applications of the HERMES model: June-October 2010,*" LLNL report LLNL-TR-462751, November 2010.

Reaugh, J. E. and E. L. Lee, "Isochoric burn, an internally consistent method for the reactant to product transformation in reactive flow," *Proceedings, 12th International Detonation Symposium*, San Diego, CA, August 2002, p504.

Reaugh, J. E. and A.G. Jones, "Mechanical Damage, Ignition, and Burn: Experiment, Model Development, and Computer Simulations to Study High-Explosive Violent Response (HEVR)," in *Proceedings, 14th International Symposium on Detonation*, Coeur d'Alene, ID, April 2010, p909.

Reaugh, J. E., E. L. Lee, and J. L. Maienschein, "*The production of Airblast from Solid Rocket Motor Fallbacks,"* LLNL report LLNL-TR- 581412, September 14, 2012.

Reaugh, J. E., J. P. Curtis, and M.-A. Maheswaran, "Computer Simulations to Study the Effects of Explosive Energetic and Constitutive Properties on the Deflagration-to-Detonation Transition (DDT)," *Proceedings, 15th International Detonation Symposium*, San Francisco, CA, July 2014. p996.

Reaugh, J. E., J. P. Curtis, and M.-A. Maheswaran, "Modeling the Deflagration to Detonation Transition in porous PETN of Density 1.4 g/cc with HERMES, *AIP Conf. Proc. TBD* (St. Louis, MO) 2018, to be published.

Roessig, K. M. and J.C. Foster, Jr., "Experimental Simulations of Dynamic Stress Bridging in Plastic Bonded Explosives," *Proceedings of the Conference of the American Physical Society Topical Group on Shock Compression of Condensed Matter*, Atlanta, GA, June 24-29, 2001, p829.

Terzaghi, K., R. B. Peck, and G. Mesri, *Soil Mechanics in Engineering Practice*, 3d Edition, Wiley, New York, 1996.

Tringe, J. W., E. A. Glascoe, M. A. McClelland, D. Greenwood, R. D. Chambers, H. K. Springer, and H. W. Levie, "Pre-ignition confinement and deflagration violence in LX-10 and PBX 9301," *J. Appl. Phys.*, **116**, 054903 (2014)

Tringe, J. W., K. S. Vandersall, H. W. Levie, R. F. Hanson, L. B. Smilowitz, and G. R. Parker, "Observations and Modeling of the Deflagration-to-Detonation Transition (DDT) in Low Density HMX," *AIP Conf, Proc*. **1793**, 060024 (2017).

Vorobiev, O. Yu., B.T. Liu, I.N. Lomov, T.H. Antoun, "Simulation of penetration into porous geologic media," *Int. J. Impact Engineering*, **34**, p721, April 2007.

White, B. W., H. K. Springer, and J. E. Reaugh, "Computational Studies of the Skid Test: Evaluation of the Non-shock Ignition of LX-10 Using HERMES," J. Physics Conf. Series 500, 192021 (2014)

Wiegand, D. A., B. Reddingius, K. Ellis, C. Leppard, "Pressure and friction dependent mechanical strength – cracks and plastic flow," *Int. J. Solids and Structures*, **48**, June 2011, p1617.

Wilkins, M. L., R. D. Streit, and J. E. Reaugh, *Cumulative-Strain-Damage Model of Ductile Fracture: Simulation and Prediction of Engineering Fracture Tests*, Lawrence Livermore National Laboratory report UCRL-53058, October 1980.

Wilkins, M. L., *Computer Simulation of Dynamic Phenomena*, Springer-Verlag, Berlin, 1999.

Zehnder, A. T., *Fracture Mechanics*, Lecture Notes in Applied and Computational Mechanics 62, Dordrecht: Springer Netherlands, 2012.

Zywich, E. private communications, LLNL, summer and fall 2013.